Polypyrrole-promoted rGO-MoS_2 nanocomposite for enhanced photocatalytic conversion of CO_2 and H_2O to CO, CH_4 and H_2 products

Neeraj Kumar[1*], Santosh Kumar[2], Rashi Gusain[1,3], Ncholu Manyala[4], Salvador Eslava[2] and Suprakas Sinha Ray[1,3*]

[1]Centre for Nanostructures and Advanced Materials, DSI-CSIR Nanotechnology Innovation Centre, Council for Scientific and Industrial Research, Pretoria 0001, South Africa

[2]Department of Chemical Engineering, Imperial College London, London, SW7 2AZ, United Kingdom

[3]Department of Chemical Sciences, University of Johannesburg, Doornfontein 2028, South Africa

[4]Department of Physics, Institute of Applied Materials, SARChI Chair in Carbon Technology and Materials, University of Pretoria, Pretoria 0002, South Africa

*Corresponding authors: N. Kumar (nkumar@csir.co.za; ynk.neeraj@gmail.com), and S. S. Ray (rsuprakas@csir.co.za; ssinharay@uj.ac.za)

ORCID id-

Neeraj Kumar: 0000-0001-5019-6329

Suprakas Sinha Ray**:** 0000-0002-0007-2595

Graphical abstract

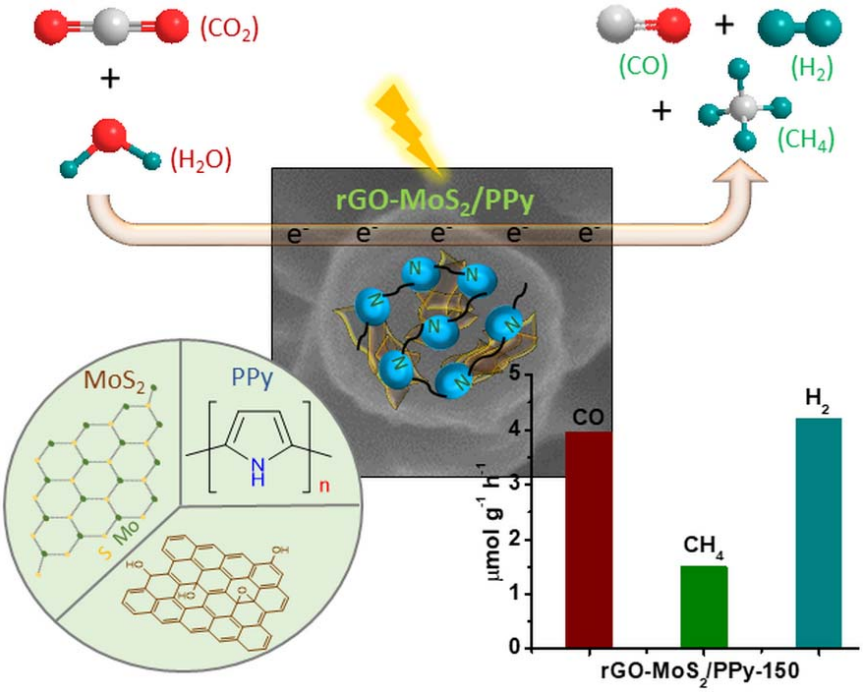

Abstract

Advanced functionalized nanomaterials are indispensable for the efficient production of solar fuels via the reduction of CO_2 under solar light. This approach simultaneously addresses two major issues: (a) global warming due to anthropogenic CO_2 production and (b) the ongoing energy crisis. Owing to their high catalytic activity and visible light absorption, MoS_2 has recently emerged as a suitable candidate for the photocatalytic production of solar fuels from water splitting and CO_2 reduction. However, it currently shows poor conversion efficiency due to low adsorption of reactant gases, fast radiative recombination, and low chemical stability; these factors limit their practical applicability. In this work, CO_2 photoreduction and H_2 production were enhanced by integrating photoabsorber MoS_2 and N-containing conducting polymer polypyrrole (PPy) on reduced graphene oxide (rGO). rGO-MoS_2/PPy nanocomposites with various amounts of PPy were fabricated and morphologically, structurally, and optically characterized using several techniques. The optimal rGO-MoS_2/PPy nanocomposite was found to exhibit a remarkable production of CO (3.95 μmol g^{-1} h^{-1}), CH_4 (1.50 μmol g^{-1} h^{-1}), and H_2 (4.19 μmol g^{-1} h^{-1}) in the photocatalytic reduction of CO_2 in an aqueous suspension under simulated sunlight. The enhanced photocatalytic performance of the nanocomposites was attributed to the beneficial combination of the rGO skeleton, MoS_2 nanosheets, and *in-situ* polymerized conductive PPy; this effectively promoted charge transfer, delayed recombination, improved light absorption and CO_2 adsorption. In summary, this study describes an inexpensive non-noble metal photocatalyst with three components for the efficient photoreduction of CO_2 into clean solar fuels.

Keywords: *CO_2 Photoreduction; Polypyrrole; MoS_2; Reduced graphene oxide; 2D materials; Hydrogen production*

1. Introduction

The industrial revolution, fossil fuel consumption, transportation vehicles and other human activities are primarily responsible for the increasing concentration of atmospheric CO_2 and the resulting threat of climate change. CO_2 is one of the primary greenhouse gases, which continue to contribute to global warming. According to the International Panel on Climate Change (IPCC) report, the CO_2 concentration in the environment will reach 590 ppm by 2100; this will lead to a significant increase in the global temperature by 1.96 °C.[1] Therefore, concerns over the increasing concentration of CO_2, exhaustion of fossil fuels, and detrimental effects of CO_2 on the environment are growing worldwide. Several methodologies for alleviating the accumulation of CO_2 in the environment and the energy crisis have been proposed: (a) carbon capture and utilization (CCU) of CO_2 in various applications, (b) the use of alternative carbon-free energy sources, and (c) the photo/electro-conversion of CO_2 into value-added chemicals and fuels such as carbon monoxide (CO), methane (CH_4), methanol (CH_3OH), formic acid (HCOOH) and other hydrocarbons.[2-3] However, CO_2 is an inert and thermodynamically stable molecule, and its photoreduction is energetically unfavorable. The sustainable and economical photoreduction of CO_2 can be performed in an aqueous medium under solar irradiation using advanced heterogeneous photocatalysts that mimic the natural photosynthesis process to produce solar fuels in an eco-friendly way.[3-4] The simultaneous photocatalytic water splitting and CO_2 reduction to produce solar fuels is considered to be a critical sustainable methodology to alleviate the problem of anthropogenic climate change but remains an enormously challenging task.[5] Several nanomaterials, including as g-C_3N_4, metal oxides (*viz.* TiO_2), metal sulfides, carbon-based materials, metal-organic frameworks (MOFs), and nanocomposites have been investigated for use as photocatalysts to reduce CO_2 into value-added chemicals.[6-12]

To achieve high efficiency, a semiconductor material should exhibit several features: (a) fast charge transfer, (b) suitable conduction and valence band edges, (c) active surface sites that allow adsorption of the reactants and easy desorption of the products to avoid further photo-oxidation, (d) photoactivity under the visible spectrum of solar light, and (e) null or slow recombination of photoinduced charge pairs.[13] Recently, two-dimensional (2D) layered nanomaterials such as graphene, graphene oxide, metal dichalcogenides, layered double hydroxides (LDHs), g-C_3N_4, and inorganic perovskites have attracted immense interest as photocatalysts, sensors, solar cells and supercapacitors due to their outstanding characteristics, such as excellent specific surface area, enhanced conductivity, porous structure, improved charge pair separation, ease of functionalization with co-catalysts, stability, and excellent light-harvesting properties.[14-20] MoS_2 has also received a significant amount of interest for adsorption, lubrication, catalysis, energy storage, medical, and fire retardant applications due to its abundance, accessible cost, and remarkable chemical, physical, optical, and interlayer properties.[21-28] In particular, MoS_2 exhibits a strong solar light absorption potential due to its narrow bandgap and can adjust its conduction band edge by altering the number of layers via quantum confinement effects; these properties have rendered it famous in a variety of photocatalytic applications.[21, 29] However, the fast recombination of photogenerated charge pairs in MoS_2 limits its practical application. Several strategies have been attempted to fabricate nanocomposites of MoS_2 with other conducting materials to enhance its activity by improving its charge transfer rate and delaying charge pair recombination.[29-30]

Taking advantage of the high surface area, high aspect ratio and excellent conductive properties of reduced graphene oxide (rGO), Chen et al. prepared a MoS_2-rGO nanocomposite that exhibited improved photocatalytic activity in the photo-degradation of organic dyes.[31-32] Liu et al. also reported the high active site density, excellent conductivity, stability in acidic media, and improved catalytic activity of MoS_2/rGO nanocomposites.[33] Recently, several

reports of the synthesis strategies and application of MoS_2/rGO nanocomposites have been published; their performance in electrocatalysis, HER evolution and photodegradation applications were found to be superior to that of pristine GO and MoS_2.[31, 34] Conducting polymers such as polyaniline, polypyrrole, and polythiophene have attracted a great deal of interest in nanocomposite design as surface capping agents; these polymers also represent right hole conducting materials to improve charge transfer and mitigate recombination. In nanocomposites of conducting polymer with inorganic nanomaterials, the excellent conductivity of the conducting polymer and the unique optical and electrical characteristics of inorganic materials can be exploited in photocatalysis.[35-36]

In this work, we demonstrate the construction of an rGO-MoS_2 nanocomposite with polypyrrole (PPy) via a hydrothermal method for enhanced photocatalytic reduction of CO_2 with H_2O to CO, CH_4 and H_2 products. The chemical and morphological changes in the nanocomposite were studied using X-ray diffraction (XRD), Raman spectroscopy, X-ray photoelectron spectroscopy (XPS), and electron microscopy. Photoluminescence (PL) and UV-vis spectroscopy analyses were used to study the optical characteristics of the rGO-MoS_2/PPy nanocomposites. The effect of the PPy content of the rGO-MoS_2/PPy nanocomposite on the reduction of CO_2 under light irradiation was studied, and the performance of the rGO-MoS_2/PPy nanocomposites was compared with that of MoS_2 and rGO-MoS_2 to elucidate the benefits of adding PPy.

2. Experimental Section

2.1. Materials

Graphite powder (powder, <20 μm, synthetic), sodium molybdate dihydrate (≥99.5%), thiourea (≥99.0%), pyrrole (98%), hydrogen peroxide solution (H_2O_2 30% w/w in H_2O), hydrochloric

acid solution (HCl, 32 wt. % in H_2O), potassium persulphate (KPS, ≥99.0%) and sodium bicarbonate ($NaHCO_3$, ≥99.7%) were purchased from Sigma-Aldrich and used as received in reactions.

2.2. Synthesis of reduced graphene oxide-molybdenum disulfide (rGO-MoS_2) nanocomposite

Graphene oxide (GO) was synthesized via the improved Hummers' method[37] as explained in the supplementary information. The synthesized GO was then used for the preparation of the reduced graphene oxide-molybdenum disulfide nanocomposite (33 wt% of rGO in rGO-MoS_2) nanocomposite via a facile hydrothermal method. In brief, 0.5 g sodium molybdate was added to 140 mL of an aqueous dispersion containing 250 mg of GO and sonicated for 15 minutes. Subsequently, 0.9 g thiourea was dissolved in 10 mL distilled water and added to the above mixture, which was then stirred at room temperature for 20 min. The mixture was then transferred to a Teflon-lined stainless-steel autoclave and subjected to heating treatment at 200 °C for 24 h. The hydrothermal reaction mixture was allowed to cool to room temperature, and the resulting black precipitate was collected by centrifugation at 4,000 rpm for 15 min. The collected rGO-MoS_2 nanocomposite was washed several times with distilled water to remove impurities and undigested chemicals, and dried in an oven at 70 °C overnight. For the synthesis of the MoS_2 nanosheets, the reaction was carried out as above, but without using GO.

2.3. Synthesis of the rGO-MoS_2/PPy nanocomposites

100 mg of the synthesized rGO-MoS_2 was dispersed in 150 mL distilled water via ultrasonication in a bath sonicator for 30 min. After the ultrasonic treatment, 600 μL pyrrole was added dropwise to the rGO-MoS_2 dispersion, which was then stirred for 30 minutes at room temperature. Subsequently, the reaction was transferred to an ice bath (0-5°C). Once the temperature of the reaction reached 0-5°C, a solution of 1.2 g potassium persulfate (KPS) in distilled water (10 mL) was added dropwise to the mixture under vigorous stirring. Here, KPS

acted as an oxidant and initiated the polymerization reaction. The polymerization reaction was continuously stirred in the ice bath for 12 h. The synthesized product was collected by centrifugation at 4000 rpm for 10 min and washed with distilled water several times. The collected rGO-MoS_2/PPy nanocomposite was then dried in a vacuum oven at 65°C for 24 h. The rGO-MoS_2/PPy synthesis was repeated using 300 and 150 µL pyrrole, rather than 600 µL. The nanocomposites were labelled rGO-MoS_2/PPy-600, rGO-MoS_2/PPy-300, and rGO-MoS_2/PPy-150 according to the use of 600, 300, and 150 µL pyrrole, respectively.

2.4. Characterization

The crystalline structure and phase purity of the synthesized samples were investigated using XRD (PAN analytical X-pert PRO, Netherlands). All XRD patterns were recorded at a scan rate of 0.02° s^{-1} in the 2θ range 5-90° using Cu Kα radiation (λ = 0.154 nm) as X-ray source, operating at a current and voltage of 40 mA and 45 kV, respectively. Fourier transform infrared (FTIR) analysis of the nanomaterials was performed using a Perkin-Elmer spectrometer (model: Spectrum 100, USA) with KBr (FTIR grade) as a reference with a spectral resolution of 4 cm^{-1}. Each sample was finely ground with KBr (FTIR grade) using a mortar and pestle and pressed into a pellet. The FTIR experiment was conducted in transmittance mode over the range 4000-400 cm^{-1}. The chemical composition, binding energies, and oxidation states of the elements in the as-prepared samples were determined using XPS (Kartos, UK). All XPS spectra were collected using a monochromated Al Kα X-ray source. All the obtained XPS peaks were fitted using Gaussian functions and Shirley background correction. The specific surface areas and porosities of the synthesized materials were determined from the nitrogen adsorption and desorption isotherms using the multi-point Brunauer-Emmett-Teller (BET) technique and a Micromeritics (ASAP 2020, USA) analyzer. The surface morphologies and micro-structures of the nanocomposites were characterized using a field-emission scanning electron microscope (FESEM, Auriga FESEM, Carl Zeiss, Germany). The elemental distribution of the samples

was determined using an Oxford energy dispersive X-ray spectrometer (EDS, Oxford, UK) coupled with the FESEM. The nano-structural features of the samples were characterized using high-resolution transmission electron microscopy (HR-TEM; JEOL, 2100-JEM Japan) at the operating voltage of 200 kV. For the HR-TEM measurements, the samples were dispersed in ethanol and drop-casted on a carbon-coated grid. Elemental mapping was performed using EDS (Thermo Scientific, USA) coupled with the HRTEM. Raman analysis was carried out using an Alpha 300RAS Plus (WiTec Focus Innovations, Germany) confocal micro-Raman spectrometer with 532 nm laser excitation operated at 5.0 mW using a 50× magnifying lens. UV-vis spectroscopy was carried out using LAMBDA 750 UV-Vis-NIR Spectrophotometer, (PerkinElmer, USA).

2.5. Photocatalytic study

In order to evaluate the photocatalytic activity of the synthesized materials, CO_2 photocatalytic reduction experiments were carried out in a 125 mL stainless-steel photoreactor with quartz window for light irradiation. In a typical experiment, 50 mg catalyst was dispersed in 0.5 M $NaHCO_3$ (20 mL, pH = 7) under magnetic stirring at room temperature. Prior to light irradiation, the photoreactor was purged with He (20 mL min^{-1}, 1 h), and followed by high purity CO_2 (1 bar, 5 mL min^{-1}) purging for 1 h. The reactor was subsequently sealed and placed under a Xe lamp (300 W) equipped with an AM 1.5 G filter for 4 h with continuous stirring. The light intensity was 1 sun (100 mW/cm^2) in the sample position. Figure S1, Supporting Information, shows the spectral data graph for 300 W Xe lamp. After 4 h of light irradiation, 1 mL of the gaseous product was extracted from the photoreactor and quantitatively analyzed using a gas chromatography with a barrier ionization detector (Shimadzu GC-2030) and He carrier gas. In order to determine the effects of various experimental factors, control experiments were run in the absence of light, CO_2 (substituting CO_2 for N_2), water and catalyst. The recyclability of the photocatalyst was determined by collecting the catalyst after each run,

washing it thoroughly using distilled water, and utilizing it for another cycle of CO_2 photocatalytic reduction.

Apparent quantum efficiency (AQE) was measured under the same experimental setup, using 523 nm LED monochromatic light and the equation as follows:

$$\text{AQE} / \% = \frac{\text{Number of reacted electrons}}{\text{Number of incident photons}} \times 100$$

The detail calculation of apparent quantum efficiency (AQE) has explained in Supporting Information page S2.

3. Results and Discussion

3.1. Structural and morphological characterization

The rGO-MoS_2/PPy nanocomposites were prepared via the polymerization of pyrrole onto the surface of rGO-MoS_2 using KPS as oxidant. Formation of PPy onto rGO-MoS_2 readily covers the surface of the nanocomposite material. The XRD pattern of MoS_2 (Figure 1a) exhibits characteristic peaks at 14.15, 28.89, 33.16, 36.31, 39.74, 43.56 and 57.88°, which correspond to the (002), (004), (100), (101), (103), (006) and (110) diffraction planes, respectively, confirming MoS_2 hexagonal crystal structure (JCPDS No. 37-1492).[22] Figure S2 (Supporting Information) presents the typical GO diffraction peak at 11.12°, which corresponds to the (002) plane with an interlayer distance of 0.84 nm. Pristine graphite exhibits an interlayer spacing of 0.34 nm with a characteristic diffraction peak at 27°.[38] The significant increase in the d-spacing of the GO nanosheets was due to the oxygen functional groups present on the surface of the GO after oxidation, water molecules trapped between the layers, and ultrasonic exfoliation, which weakened the van der Waals interactions between the layers. The diffraction peak at 42.48° with a d-spacing of 2.25 nm is representing the (100) reflection with short-range order

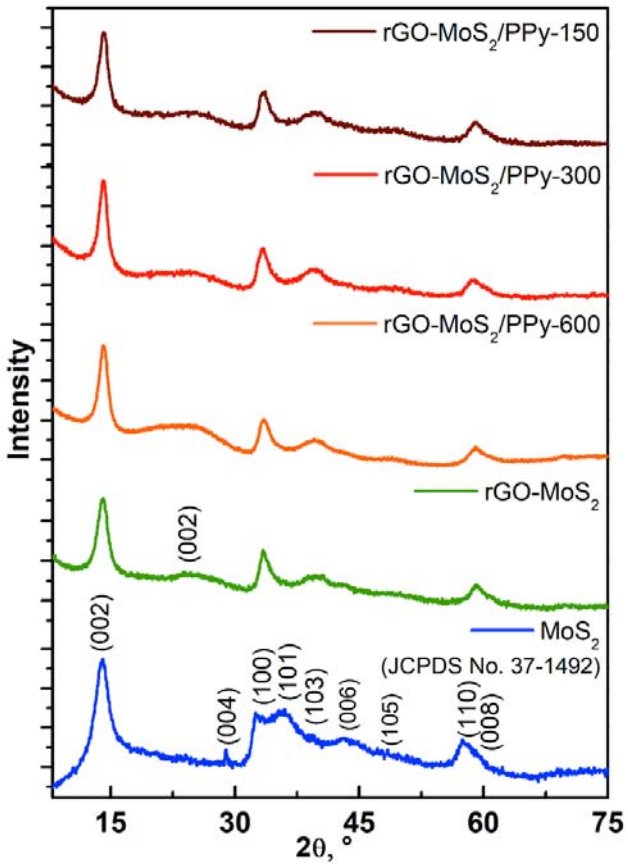

Figure 1. XRD diffractograms of (a) MoS_2, (b) rGO-MoS_2, and (c) rGO-MoS_2/PPy-600, (d) rGO-MoS_2/PPy-300, and (e) rGO-MoS_2/PPy-150 nanocomposites.

in the stacked graphene oxide layers.[39] No XRD peaks were observed at ~11 or ~42 ° in the XRD spectrum of rGO-MoS_2, confirming the reduction of GO into rGO (Figure 1b). Furthermore, the presence of a broad peak at ~25.7 ° corresponds to the (002) plane of rGO and indicates the low concentration of rGO (~5% wt) in the nanocomposites. The XRD pattern of rGO-MoS_2 shows the characteristic diffraction peaks of hexagonal MoS_2, providing evidence for the successful anchoring of MoS_2 onto the rGO sheets. The small shift in 2θ value of MoS_2 peaks in rGO-MoS_2 occurs due to intercalation of rGO into the MoS_2 sheets.[40] In addition to the MoS_2 diffraction peaks, XRD diffractograms of the rGO-MoS_2/PPy nanocomposites also exhibit a wide and weak diffraction at 2θ = 18-28°, which is a

characteristic signature of amorphous polypyrrole.[41] In the nanocomposites, the XRD broad peak of rGO was convoluted with the PPy XRD broad peak. The intensity of the PPy peak progressively decreased in the patterns of rGO-MoS_2/PPy 0.5 and rGO-MoS_2/PPy 0.25 relative to that in the rGO-MoS_2/PPy 1 pattern (see Figure 1) due to the lesser concentration of PPy in these nanocomposites.

Raman spectroscopy was used to explore the structural changes and vibrational modes in MoS_2, rGO-MoS_2 and the rGO-MoS_2/PPy-150 nanocomposite. As shown in Figure 2, MoS_2, rGO-MoS_2, and the rGO-MoS_2/PPy-150 spectra all exhibited two characteristic bands in the range 370-405 cm^{-1}, which were assigned to the in-plane ($^1E_{2g}$) vibrations of the two S atoms on Mo and the out-of-plane (^1A_g) vibrational modes of the S atoms in opposite directions, respectively, in hexagonal MoS_2.[26] Moreover, the lower intensity of $^1E_{2g}$ vibrational mode relative to the ^1A_g mode suggests the formation of edge-terminated nanosheets on rGO.[40] Generally, graphite exhibits two distinctive peaks in the Raman spectrum at ~1350 and ~1580 cm^{-1}, which are associated with the D and G bands, respectively.[42] The D band of Raman spectrum of graphite is related to the defects present in the graphite lattice, while the G band is associated with the first-order scattering of the E_{2g} vibrational mode. In the Raman spectra of rGO-MoS_2 and rGO-MoS_2-PPy, D and G bands were observed at ~1358 and ~1586 cm^{-1}. The shifting in D and G values indicate the presence of rGO in composites, which differs from GO in having more C sp^2 domains and less C sp^3 atoms.[42] However, the D and G band area of the Raman spectrum of rGO-MoS_2/PPy displayed noisy rather than clear peaks. The spectrum of pristine PPy exhibited 5 individual peaks at ~1325, ~1550, ~1040, ~920, and ~985 cm^{-1}, which corresponded to the ring and C-N stretching, π-conjugated structure, in-plane C-H deformation, out-of-plane C-H deformation, and pyrrole ring deformation, respectively. In the spectrum of rGO-MoS_2/PPy, the two major peaks of PPy overlap with the rGO Raman bands; other weak

peaks in the spectrum confirmed the presence of the polypyrrole coating on the surface of rGO-MoS_2.

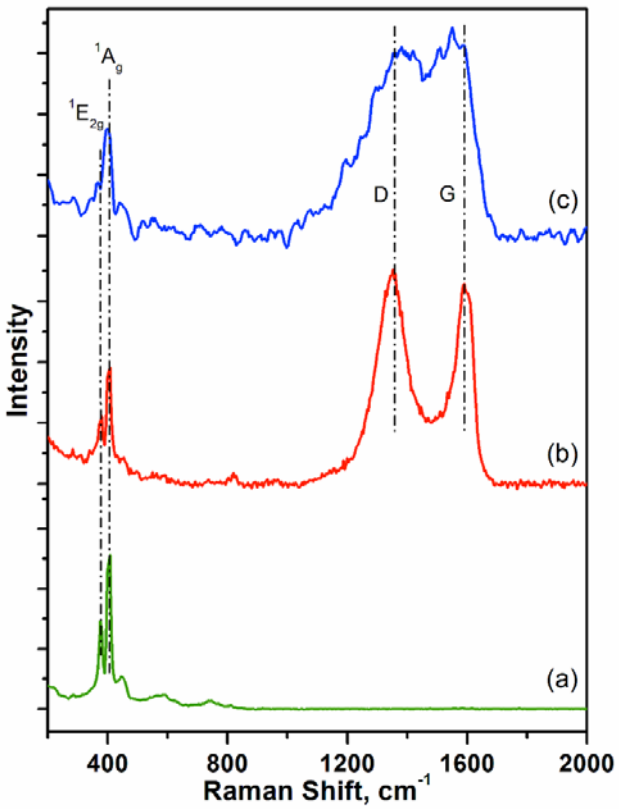

Figure 2. Raman spectra of MoS_2 (a), rGO-MoS_2 (b), and the rGO-MoS_2/PPy-150 nanocomposite (c).

In order to determine the functional moieties present in the rGO-MoS_2/PPy nanocomposites, their FTIR spectra were measured in the range 400-4000 cm^{-1} (Figure 3a). In rGO-MoS_2 FTIR spectrum (Figure S3, Supporting information), the peaks at 3432, 1711, 1223, and 1050 cm^{-1} corresponded to –OH (hydroxyl), C=O (carboxyl), C-OH and C-O (epoxy) groups of rGO, and peak at 463 cm^{-1} was ascribed to Mo-S stretching of MoS_2. These peaks confirmed the successful formation of rGO-MoS_2 composite.[26, 38] In the FTIR spectra of rGO-MoS_2-PPy nanocomposites (Figure 3a), the broad vibrational peaks around at 3423 and 3112 cm^{-1} were attributed to O-H/N-H and aromatic C-H stretching, respectively.[43] The peak at 1710 cm^{-1} was ascribed to the stretching of the residual carbonyl groups (-C=O) of rGO.[44] The strong vibration

bands at 1560 and 1465 cm^{-1} were attributed to the antisymmetric and symmetric modes of the pyrrole backbone of PPy.[45] The vibrational band at ~1560 cm^{-1} was associated with the stretching of C=C bonds in PPy and rGO in the rGO-MoS_2-PPy nanocomposites.[46] The peak at 1327 cm^{-1} was assigned to the C-N stretching of PPy. The intense peaks at 1194, and 924 cm^{-1} were associated with the PPy doping state.[42] The peak at 1053 cm^{-1} represented the -C-H deformation vibrations of the pyrrole ring. The peaks centered at 796 and 616 cm^{-1} were ascribed to out-of-plane C-H bending and C=C bending of the aromatic rings in the nanocomposite. The low intensity peak at 462 cm^{-1} corresponded to Mo-S stretching, reaffirming the presence of MoS_2 in the nanocomposite.

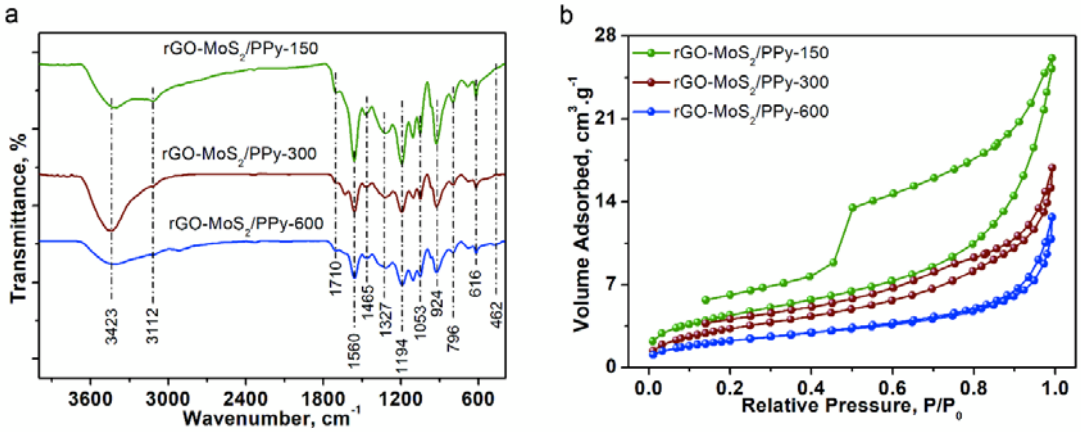

Figure 3. (a) FTIR spectra, and (b) N_2 adsorption-desorption isotherms of the rGO-MoS_2/PPY-600, rGO-MoS_2/PPy-300, and rGO-MoS_2/PPy-150 nanocomposites.

Figure 3b presents the N_2 adsorption-desorption isotherms of the rGO-MoS_2-PPy nanocomposites, which were used to calculate their BET surface area. The N_2 adsorption-desorption isotherms of MoS_2 and rGO-MoS_2 are shown in Figure S4 (Supporting Information). All the N_2 isotherms shown in Figure 3b, and Figure S4 (Supporting Information) were identified as a combination of type II and type IV isotherms with H3-hysteresis loops.[47-48] MoS_2 and rGO-MoS_2 show a BET surface area of 16.1 and 149.6 $m^2\ g^{-1}$ (Table S1, Supporting Information). Addition of PPy lowers the surface area, retaining the highest value

of 16.02 m^2/g for rGO-MoS_2/PPy-150 and 8.43 m^2/g for rGO-MoS_2/PPy-600. The obtained N_2 isotherms pattern of rGO-MoS_2/PPy composites were similar to previous studies.[49-50] In the rGO-MoS_2/PPy-150 nanocomposite, the pores had narrow necks that result in nitrogen cavitation during the desorption (kink at 0.45-0.5 P/P_o).[51] These narrow necks were, anyway, not expected in the final application due to the dispersion of the nanocomposite in 20 mL aqueous $NaHCO_3$. As adsorption is a critical first step in CO_2 photocatalytic reduction, CO_2 physisorption was carried out on the prepared samples (Figure 4). MoS_2 nanosheets physisorbed 2.8 $cm^3\ g^{-1}$, while rGO-MoS_2, rGO-MoS_2/PPy-150, rGO-MoS_2/PPy-300 and rGO-MoS_2/PPy-600 physisorbed 6.0, 10, 12 and 13 $cm^3\ g^{-1}$, respectively. These results indicate superior CO_2 adsorption with the use of rGO and PPy.

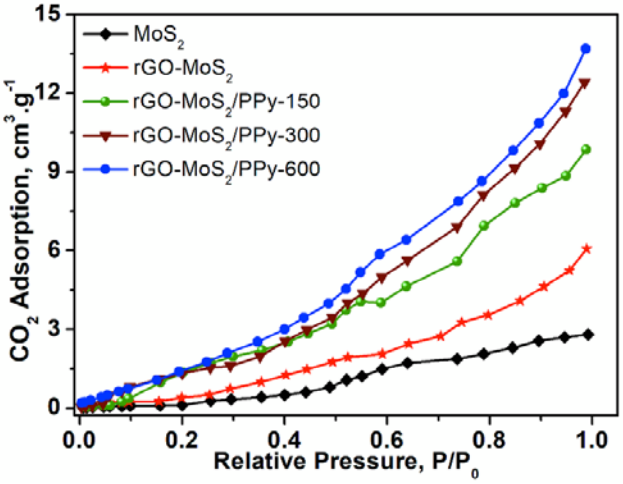

Figure 4. CO_2 adsorption of the MoS_2 nanosheets, rGO-MoS_2, rGO-MoS_2/PPy-600, rGO-MoS_2/PPy-300, and rGO-MoS_2/PPy-150 nanocomposites.

The surface morphologies of MoS_2, rGO-MoS_2, and the rGO-MoS_2/PPy nanocomposites were inspected using FESEM. The SEM micrograph in Figure 5a reveals the sheet-like morphology of MoS_2, with a thickness of approximately 10 nm and a lateral length of about 600 nm. After the addition of GO, the original sheet pattern and a lateral length of the MoS_2 nanosheets was retained, but the thickness of the sheets clearly increased (Figure 5b and inset). The increased

thickness was attributed to the anchoring of rGO nanosheets on both sides of basal planes of the pristine MoS_2 nanosheets. Granular spherical structures with a size of 200-300 nm were observed after the introduction of pyrrole in the as-prepared rGO-MoS_2 system (Figure 5c-f). According to the literature, pyrrole has a tendency to form spherical structures on polymerization using an oxidizing agent such as $FeCl_3$ or ammonium persulphate.[45, 52-53] Here, the PPy nanospheres were grown on the available wide surface of rGO-MoS_2 nanosheets. As shown in Figure 5c-d, the nanospheres of the rGO-MoS_2/PPy-150 nanocomposite were interconnected, and as the concentration of PPy was increased, the sphere-like structures became more irregular and aggregated (Figure 5e-f). Furthermore, EDS mapping (Figure 5g) indicated that the elements C, N, Mo, O, and S were distributed uniformly throughout the rGO-MoS_2/PPy-150 nanocomposite, the EDS spectrum (Figure S4 5, Supporting Information) also confirmed the successful formation of the nanocomposite. The homogenous distributions of N and C, as well as Mo and S, further confirmed the presence of PPy in the rGO-MoS_2/PPy-150 nanocomposite.

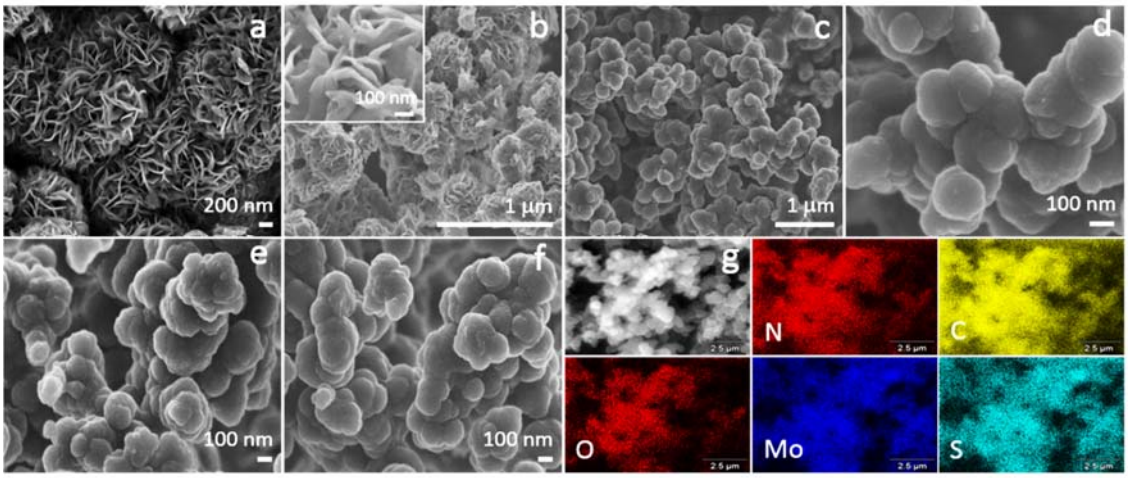

Figure 5. FESEM micrographs of (a) MoS_2, (b and inset) rGO-MoS_2, (c-d) rGO-MoS_2/PPy-150, (e) rGO-MoS_2/PPy-300, (f) and rGO-MoS_2/PPy-600 (f) nanocomposites. (g) The micrograph selected for the EDS measurement of the rGO-MoS_2/PPy-150 nanocomposite and its N, C, Mo, S and O EDS maps.

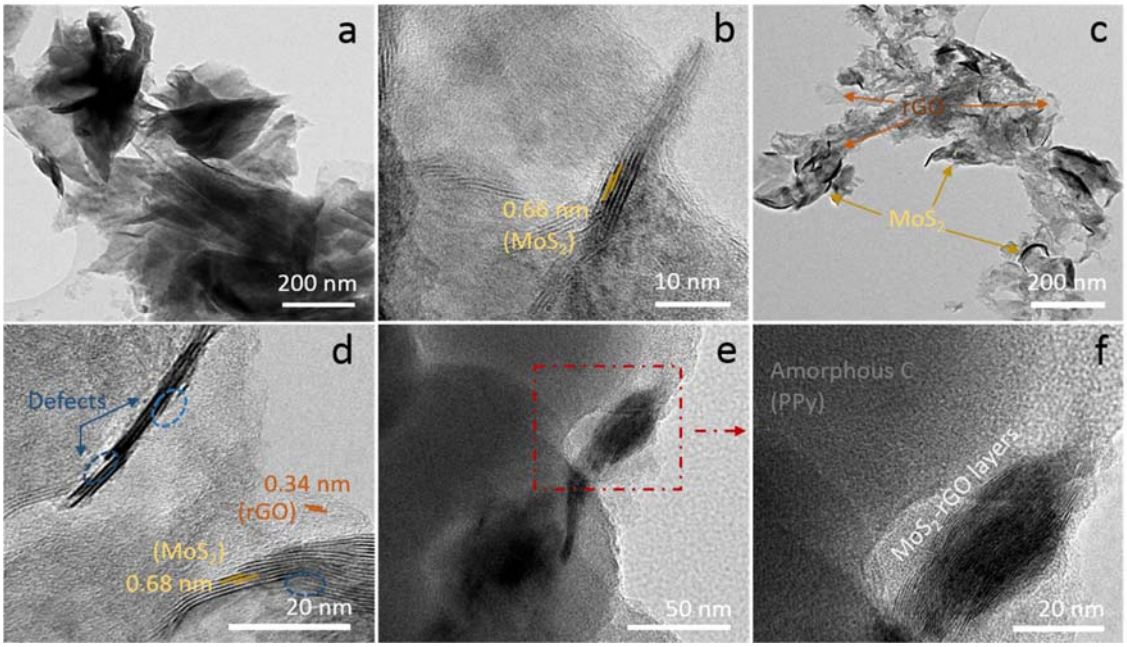

Figure 6. TEM micrographs of (a-b) MoS_2, (c-d) rGO-MoS_2, and (e-f) the rGO-MoS_2/PPy-150 nanocomposites.

Furthermore, TEM inspection was performed to examine the microstructural features of the as-synthesized materials in detail. Figure 6a shows the loose packing of the MoS_2 nanosheets, which were attached to one another via van der Waals forces. The ribbon-like MoS_2 structures consisted of flakes of 3-14 molecular lamellae (Figure 6b) with an interlayer spacing of 0.66 nm, which was very similar to the characteristic interlayer distance of 0.616 nm for the hexagonal 2H-MoS_2 structure. Figure 6c reveals that MoS_2 nanosheets grew uniformly on the surface of the rGO sheets. The rGO sheets, which had lateral dimensions of a few microns, and the MoS_2 nanoflakes are indicated with arrows. Additionally, the nanosheets with an interlayer spacing of 0.34 nm and 0.68 nm in the HRTEM micrograph (Figure 6d) correspond to rGO and MoS_2, respectively, confirming the successful formation of rGO-MoS_2. The defects highlighted in Figure 6d and the abundant edge sites resulting from the high aspect ratio of rGO-MoS_2 should offer an extensive active catalytic surface for the photocatalytic reaction. Figure 6e-f are representative TEM micrographs of the rGO-MoS_2/PPy-150 nanocomposite,

demonstrating that rGO-MoS2 nanosheets homogenously surrounded the nanospheres of conducting PPy. The HRTEM micrograph further confirmed the amorphous nature of PPy in the rGO-MoS_2/PPy-150 nanocomposite (Figure 6f).

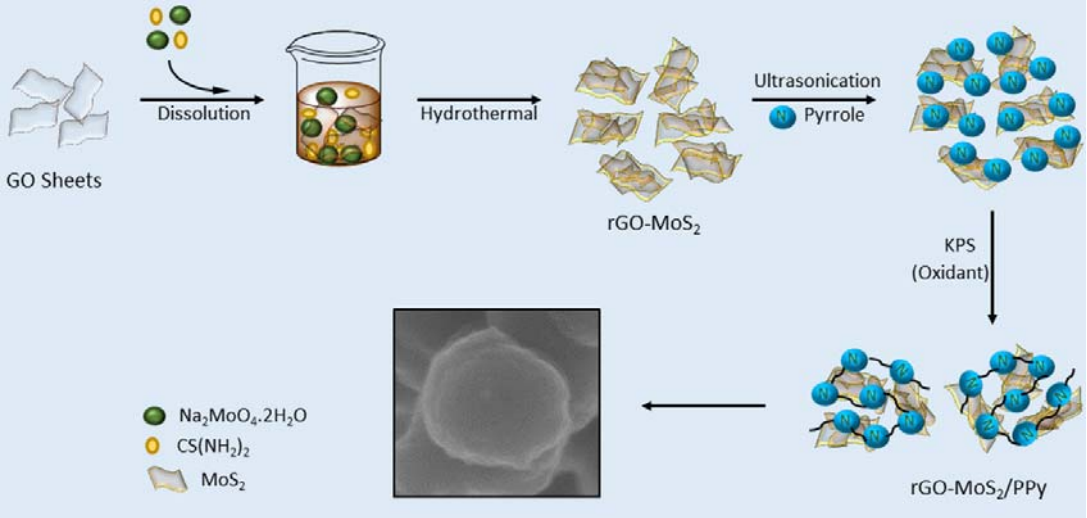

Figure 7. Schematic illustration of the preparation of the rGO-MoS_2/PPy nanocomposites.

Based on the aforementioned observations, the synthesis of the rGO-MoS_2/PPy nanocomposite was proposed to occur via the mechanism shown schematically in Figure 7. First, the GO sheets are dispersed in water, followed by the addition of the molybdenum and sulfur precursors to the suspension. The MoS_2 nuclei initially grow over the GO sheets and then self-assemble into nanosheets during the hydrothermal reduction at the same time the GO reduces to rGO. For the *in-situ* polymerization process, the rGO-MoS_2 nanosheets are dispersed in deionized water via ultrasonication, and the pyrrole monomer is then introduced into the reaction mixture. The pyrrole can adsorb onto the rGO-MoS_2 surface via electrostatic interactions between the positively charged nitrogen atoms of pyrrole, and the negatively charged surfaces of MoS_2 and rGO.[22, 54] Upon the addition of the oxidant KPS, the adsorbed pyrrole is polymerized and remains attached to the surface of rGO-MoS_2. As the conducting PPy is formed, its orientation is controlled by the rGO-MoS_2 nanosheets. Herein, rGO-MoS_2 serves as a hard

template/supporting material that provides copious active sites for the uniform growth and heterogeneous nucleation of PPy.

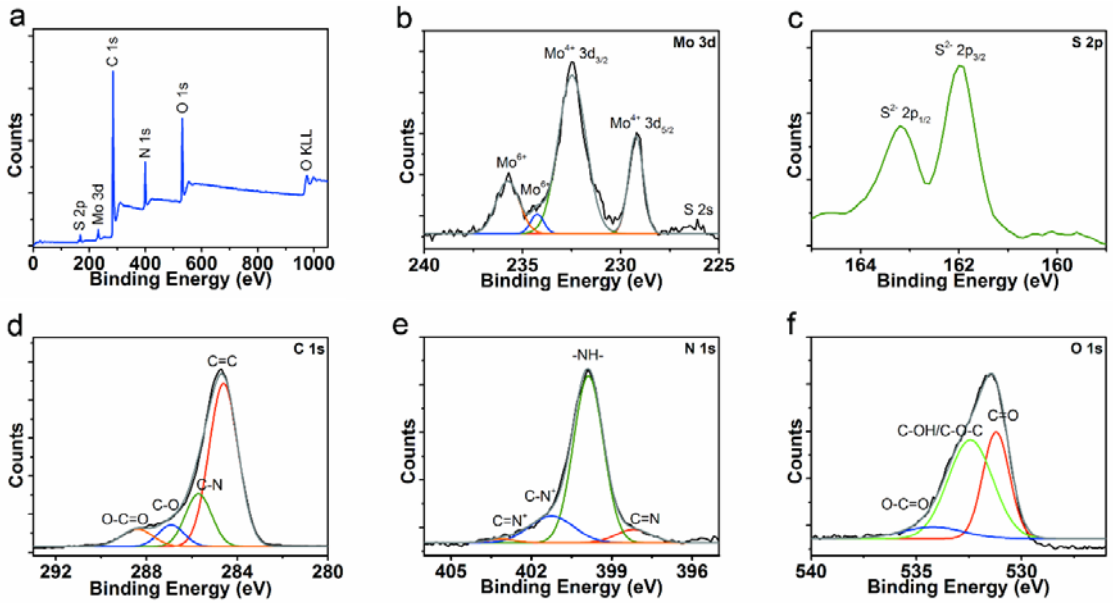

Figure 8. XPS survey spectrum (a) and high-resolution spectra of the nanocomposite rGO-MoS_2/PPy-150 (b-f).

In order to confirm the chemical states and chemical constituents of the rGO-MoS_2/PPy-150 nanocomposite, its XPS spectrum was studied (Figure 8). The survey spectrum of the rGO-MoS_2/PPy 0.25 nanocomposite clearly exhibits characteristic Mo, S, N, and O peaks, as seen in Figure 8a. In Fig 8b-f, the high-resolution Mo 3d, S 2p, N 1s, O 1s, and C 1s spectra were deconvoluted to examine the bonding in rGO-MoS_2/PPy-150. As shown in Figure 8b, the high-resolution spectrum of Mo 3d contains 4 major peaks at 229.2, 232.4, 234.1, and 235.8 eV. The deconvoluted peaks at 229.2 and 232.4 eV were ascribed to Mo^{4+} $3d_{5/2}$ and Mo^{4+} $3d_{3/2}$, respectively. The spacing between the deconvoluted peaks (~3.2 eV) due to spin-orbit splitting indicated the presence of Mo^{4+} of MoS_2 in rGO-MoS_2/PPy 0.25. The higher binding energy peaks at 233.2 and 235.7 eV were assigned to Mo^{6+} $3d_{5/2}$ and Mo^{6+} $3d_{3/2}$, respectively, which may have been present due to the insufficient reduction of MoO_4^{2-} species during the reaction. In addition, the smaller peak at 226.1 eV is related to S 2s from the MoS_2 nanosheets. The XPS

spectrum of S 2p contains two peaks at 161.9 and 163.2 eV, which were attributed to the S^{2-} $2p_{3/2}$ and S^{2-} $2p_{1/2}$ orbitals, of MoS_2 in rGO-MoS_2/PPy-150, respectively (Figure 8c). The C 1s peak can be deconvoluted into four peaks at 284.6, 285.7, 286.8, and 288.4 eV, which were ascribed to C=C/C-C, C-N, C-O, and COOH groups, respectively (Figure 8d). The high intensity of the peak centered at 284.6 eV indicated the abundance of C=C/C-C groups in the PPy and rGO of the rGO-MoS_2/PPy-150 nanocomposite. The deconvoluted peak at 285.7 eV was attributed to the C-N groups of PPy. The remaining oxygen-containing functional groups of rGO, including the hydroxyl, ketonic, ether, phenolic, and carboxylic groups were associated with the higher binding energy peaks at 286.8 and 288.4 eV. The high-resolution N 1s spectrum was deconvoluted into four peak components at 399.8, 398.1, 401.2, and 403.0 eV (Figure 8e). The deconvoluted peaks centered at 399.8 and 398.1 eV were assigned to the –NH- groups and C=N defects of PPy, respectively. The polaron ($C-N^+$) and bipolaron ($C=N^+$) arrangements of PPy were assigned to the higher binding energies at 401.2 and 403.0 eV, respectively.[55] The deconvolution of the O 1s peak is shown in Figure 8f. The singlet O 1s peak was deconvoluted into three signals at 531.2, 532.5 and 534.2 eV, which were ascribed to C=O (oxygen double bonded to aromatic C), C-OH/C-O-C (hydroxyl and ether groups of rGO), and O-C=O (carboxylic groups of rGO), respectively.[56-57]

3.2. Photocatalytic Reduction of CO_2

The performance of the synthesized materials was determined based on the photocatalytic reduction of aqueous phase CO_2 under simulated solar light. In the photocatalytic reaction, the aqueous medium acts as a reducing agent of CO_2. As shown in Figure 9a, among the different photocatalysts, the rGO-MoS_2/PPy-150 nanocomposite demonstrated the highest efficiency for the photocatalytic reduction of CO_2 to CO (3.95 μmol g^{-1} h^{-1}), CH_4 (1.50 μmol g^{-1} h^{-1}), and H_2 (4.19 μmol g^{-1} h^{-1}). More importantly, O_2 (7.10 μmol g^{-1} h^{-1}) was also generated as an oxidation product over the rGO-MoS_2/PPy-150 nanocomposite due to the concomitant hole driven water

oxidation (Figure S6, Supporting Information). The total O_2 evolved was correlated with a $(CO+H_2):O_2$ and $CH_4:O_2$ stoichiometry of 2:1 and 1:2, respectively, which is consistent with the participation of $4e^-$, $8e^-$, $2e^-$ and $2e^-$ to form O_2, CH_4, CO and H_2, respectively.[58] In terms of total electrons (e^-) consumption, rGO-MoS_2/PPy-150 nanocomposite showed a photocatalytic activity of 28.4 µmol e^- h^{-1} g^{-1}, which is almost 24 and 135 times higher than rGO-MoS_2 (1.19 µmol e^- h^{-1} g^{-1}) and MoS_2 (0.21 µmol e^- h^{-1} g^{-1}), respectively. The enhanced photocatalytic reduction of CO_2 over the rGO-MoS_2/PPy-150 nanocomposite can be attributed to the high adsorption of CO_2 (Figure 4) due to the availability of -NH groups, high active surface area, and delayed recombination of e^-/h^+ pairs.[59] No products corresponding to the photoreduction of CO_2 were generated over the pristine MoS_2 and rGO-MoS_2 nanosheets, probably due to the minimal adsorption of CO_2 on the surfaces of these catalysts, their fast charge recombination, and their poor absorption of photons for photoconversion. However, these photocatalysts showed appreciable photocatalytic activity towards the H_2 evolution reaction.

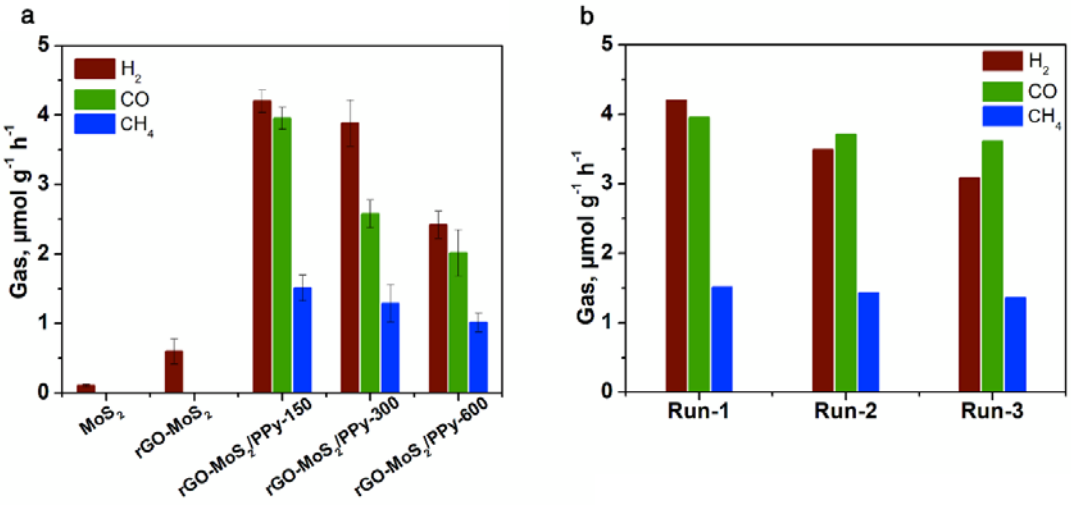

Figure 9. (a) Photocatalytic CO_2 conversion activity of MoS_2 nanosheets, rGO-MoS_2, and rGO-MoS_2/PPy nanocomposites under stimulated sunlight. (b) Reusability of rGO-MoS_2/PPy-150 nanocomposite.

Table 1: Control experiments for photocatalytic conversion of CO_2 using the rGO-MoS_2/PPy-150 nanocomposite photocatalyst.

Photocatalyst	**Reaction Gas**	**Reaction Medium**	**Simulated sunlight**	**CO, µmol g^{-1} h^{-1}**	**CH_4, µmol g^{-1} h^{-1}**	**H_2 µmol g^{-1} h^{-1}**
No Catalyst	CO_2	Aqueous	Yes	None	None	None
rGO-MoS_2/PPy-150	N_2	Aqueous	Yes	None	None	4.57
rGO-MoS_2/PPy-150	CO_2	Non-Aqueous	Yes	None	None	None
rGO-MoS_2/PPy-150	CO_2	Aqueous	None	None	None	None
rGO-MoS_2/PPy-600	CO_2	Aqueous	Yes	2.01	1.01	2.42
rGO-MoS_2/PPy-300	CO_2	Aqueous	Yes	2.58	1.29	3.88
rGO-MoS_2/PPy-150	CO_2	Aqueous	Yes	3.95	1.5	4.19

In order to confirm that detected reaction products (CO and CH_4) were produced via the photocatalysis of CO_2, control experiments (Table 1) were carried out in the absence of the photocatalyst, CO_2, aqueous medium or light irradiation. No products were obtained from the system in which CO_2 and the catalyst were combined in water under dark conditions. Similarly, no products (CO and CH_4) were evolved in the absence of CO_2, which explicitly demonstrated that CO_2 was the C source of the obtained products. In a non-aqueous medium, almost no hydrocarbons or CO were produced, demonstrating that the products were only obtained when the photocatalytic reaction over rGO-MoS_2/PPy-150 was conducted in the presence of water. These results revealed that the CO and CH_4 were produced exclusively via the photocatalytic

reduction of CO_2, and that water, light irradiation, CO_2 gas, and the photocatalyst were all-essential to the photocatalytic reaction. The main reduced product was CO; 3.95 μmol g^{-1} h^{-1} of CO was produced directly by the photocatalytic reduction of CO_2 over the rGO-MoS_2/PPy-150 nanocomposite without the use of any scavenger or cocatalyst. Moreover, the reusability and durability of the rGO-MoS_2/PPy-150 photocatalyst were assessed by using the catalyst for three successive cycles in the same reaction environment (Figure 9b). After each run, the photocatalyst was washed and the aqueous medium was replaced with a new solution. No significant decline in the CH_4 and CO evolution was observed during three successive test runs, confirming the excellent stability and durability of the nanocomposite surface during prolonged operation. After three cycles, the decline in the photocatalytic performance was occurred due to mass loss and decrease in active sites of the catalyst with time.

Furthermore, the MoS_2 nanosheets and nanocomposites were analyzed using UV-vis spectroscopy and PL measurements in order to better understand their photocatalytic behavior (Figure 10). The doublet absorption peaks at 623 and 666 nm in the UV-vis spectrum of MoS_2 were ascribed to excitonic interband transitions, which originated from the direct-gap transitions at the K point of Brillouin zone of MoS_2 (Figure 10a).[60] The doublet absorption peak originates from the spin-orbit splitting of the K point transition. The peaks positioned at 403 and 460 nm arise due to interband transition between the occupied orbital (d_z^2) and the unoccupied orbitals (d_{xy}, $d_{x^2-y^2}$, and $d_{xz,\ yz}$).[61] The obtained spectrum was similar to reported UV-vis spectra of MoS_2 nanosheets.[62-63] The peak at high wavelength is related to the direct optical band gap of 666 nm (~1.9 eV) for MoS_2, smaller than the indirect band gap of 1030 nm (1.2 eV). The absorption band at ~318 nm in the spectrum of rGO-MoS_2/PPy nanocomposite was attributed to the π-π* electron transition of the pyrrole rings of PPy,[64] whereas the broad peak at 400-600 nm was assigned to electron transfer from the highest occupied molecule orbital (HOMO) to the lowest unoccupied molecular orbital (LUMO) of PPy. Overall, the

lower content of PPy in the nanocomposite increased its visible-light absorption, which was crucial to its enhanced photocatalytic properties.[53] Moreover, the bandgap of the MoS_2 nanosheets was determined from their Tauc's plots, which were obtained by plotting the modified Kubelka-Munk function versus the photon energy (Figure S7, Supporting Information). The calculated band-gap (E_g) energy values of the MoS_2 nanosheets in MoS_2 and rGO-MoS_2 samples were ~1.90 and ~2.02 eV. The latter value is also expected for the MoS_2 nanosheets bandgap in rGO-MoS_2/PPy nanocomposites, since PPy was added after the formation of rGO-MoS_2. These values suggest that all the photocatalysts can be excited under visible light irradiation. The quantum confinement in the nanosheets in the rGO-MoS_2 sample compared with the MoS_2 sample was accountable for the increase in the band gap, which is close to single-layer results.[65]

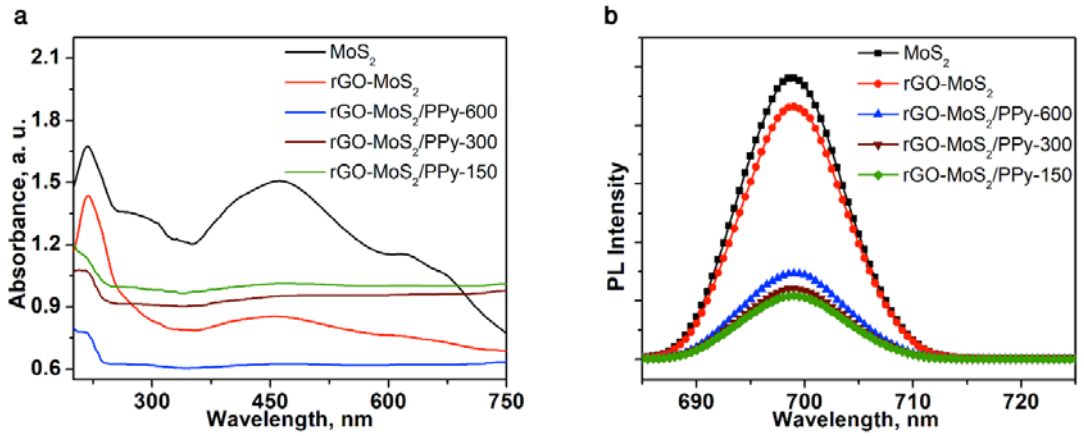

Figure 10. (a) UV-vis absorbance spectra and (b) PL spectra of the MoS_2 nanosheets, rGO-MoS_2, rGO-MoS_2/PPy-600, rGO-MoS_2/PPy-300, and rGO-MoS_2/PPy-150 nanocomposites.

Additionally, PL measurements were carried out at room temperature to predict the charge transfer and recombination rate of the photogenerated charge pairs. Figure 10b shows the PL emission of all photocatalysts (MoS_2, rGO-MoS_2, rGO-MoS_2/PPy-150, rGO-MoS_2/PPy-300, rGO-MoS_2/PPy-600) at ~698 nm due to direct-gap optical transitions on excitation at 350 nm.[66-67] The PL intensity of the rGO-MoS_2/PPy nanocomposites was lower than that of the

MoS_2 and rGO-MoS_2 nanosheets, suggesting that the coupling of PPy to rGO-MoS_2 ensured charge transfer between phases and, therefore, suppressed electron-hole recombination. The lowest PL intensity was detected for the rGO-MoS_2/PPy-150 nanocomposite, confirming that it exhibited the lowest recombination of surface charge carriers and hence it was a better photocatalyst. The aforementioned observations highlighted that the addition of PPy to rGO-MoS_2 create an interfacial contact that enhanced charge transfer and separation, and ultimately improved the photocatalytic activity towards CO_2 reduction and H_2 production.

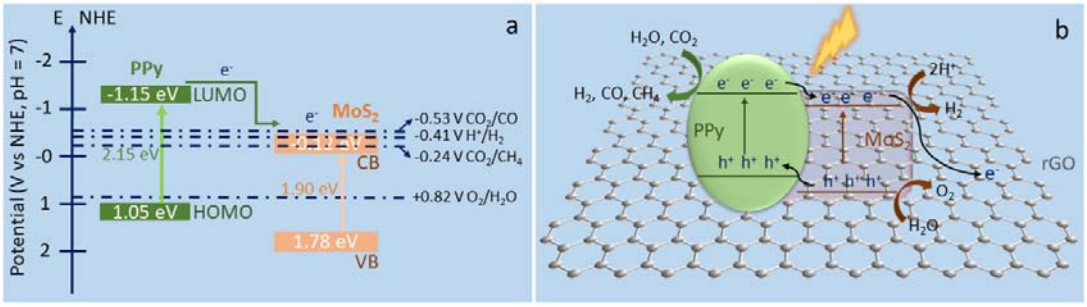

Figure 11. (a) Schematic representation of the band positions and potentials of PPy and MoS_2. (b) Mechanism of photocatalytic CO_2 conversion and water splitting on the rGO-MoS_2/PPy nanocomposite.

Based on the above discussions, a proposed mechanism for the enhanced CO_2 reduction over the rGO-MoS_2/PPy photocatalysts was proposed. Schematic illustrations of the charge segregation and transfer system in rGO-MoS_2/PPy are presented in Figure 11 a-b; first schematic shows the valence band and conduction band edges of MoS_2, and the HUMO and LUMO levels of PPy. The conduction band (E_{CB}) and valence band (E_{VB}) edge positions of the MoS_2 semiconductor were calculated by the Mulliken electronegativity theory [68]:

$$E_{\mathrm{VB}} = \chi - E_e + 0.5 \times E_{\mathrm{g}} \quad (1)$$

$$E_{\mathrm{CB}} = E_{\mathrm{VB}} - E_{\mathrm{g}} \quad (2)$$

where χ is the absolute electronegativity of MoS_2, which is calculated as 5.331. E_g is the bandgap energy. E_e is the energy of free electron on the hydrogen scale that is equal to 4.5 eV.

Based on the Eqs. (1) and (2), the E_{CB} of MoS_2 is determined as -0.12 V vs the normal hydrogen electrode (NHE), whereas the respective E_{VB} is calculated as +1.78 V vs. NHE. The potential values of HOMO and LUMO of PPy were found to be E_{HOMO} = +1.05 V and E_{LUMO} = -1.15 V, giving a HOMO-LUMO gap of 2.15 eV.[69] The rGO plays a crucial role in the segregation and transfer of photogenerated charge carriers. Owing to the appropriate positions of the band-edge potentials for water-splitting, all the photocatalysts produced H_2 ($E_{H+/H2}$ = -0.41 V vs. NHE) and O_2 ($E_{O2/H2O}$ = +0.82 V vs NHE) gas. The rGO-MoS_2/PPy nanocomposites provided the appropriate positions of the band-edge potentials for photocatalytic CO_2 conversion as well as water splitting and produced CO ($E_{CO2/CO}$ = -0.53 V vs. NHE), CH_4 ($E_{CO2/CH4}$ = -0.24 V vs. NHE) and H_2 ($E_{H+/H2}$ = -0.41 V vs. NHE) gas. However, MoS_2 and GO-MoS_2 could not reduce CO_2 to produce CO and/or CH_4 in detectable amounts, possibly due to the minimal adsorption of CO_2 on catalyst surfaces and fast charge pair recombination.

rGO-MoS_2 produced more H_2 than MoS_2, ascribed to the role of rGO as an electron acceptor and transporter to keep the generated charge pairs separated, as was also supported by PL studies.[70] All the rGO-MoS_2/PPy nanocomposites produced significant amounts of H_2, as well as enhanced production of CO and CH_4. For efficient photocatalysis, the adsorption of the reactant molecule onto the photocatalyst is a crucial step. Kim et al. prepared an N-doped porous carbon material via the chemical activation of polypyrrole-functionalized graphene and found that it efficiently adsorbed CO_2 molecules.[71] They also reported that when the concentration of nitrogen in the adsorbent was reduced, the amount of adsorbed CO_2 also decreased. They suggested that the presence of nitrogen atoms alters the bandgap and improves the electron mobility for acidic gas adsorption. This suggests that the main role of PPy in the rGO-MoS_2/PPy nanocomposite is the adsorption of CO_2 for a more efficient photocatalytic reduction. PPy can also act as a photosensitizer that introduces electrons to the CB of MoS_2 and rGO. The amount of PPy in the nanocomposite remarkably influenced the rates of the CO_2

photocatalytic reduction and hydrogen production (Fig 8). The amount of all photocatalytic reduction products, i.e., CO, CH_4, and H_2, was maximal for an optimal concentration of PPy in the nanocomposite (rGO-MoS_2/PPy-150 sample). A high PPy concentration might prevent MoS_2 from absorbing the solar spectrum visible light and, subsequently, reduce the amount of light irradiation driving the photocatalysis, so an optimal amount is required.[36]

The higher photocatalytic activity of rGO-MoS_2/PPy-150 was due to the synergistic effect of the MoS_2, rGO and PPy nanostructures in the composite. The high performance of rGO-MoS2/PPy-150 can also be associated with availability of a large number of photogenerated electrons for activation of CO_2 molecules and the formation of intermediate products, which eventually increase the quantum yield. The overall calculated AQE for rGO-MoS_2/PPy-150 is 0.30 %, which is approximately equal or higher than to reported value (Supporting Information S2).[72-74] A mechanism is herein proposed. Under visible-light illumination, the VB electrons (e^-) of MoS_2 are excited to the CB and electrons move from the HOMO of PPy to the LUMO, creating an equal number of holes (h^+) in the VB/HOMO. The photoinduced electrons react with carbonate or bent $CO_2^{\bullet-}$ species adsorbed on the surface, influencing the reduction of CO_2. The negatively charged CO_2 species are easily adsorbed on the positive metallic Mo centers and Mo-terminated edges of MoS_2 that are provided by the defects and amine sites of PPy via electrostatic attraction. The LUMOs of the negative CO_2 species adsorbed on the surface are lower than those of gaseous CO_2, making it easier for them to receive excited electrons from the photocatalysts. The photogenerated electrons in the LUMO of PPy tend to be transferred to the CB of MoS_2 due to the favorable band alignment between the two constituents. Similarly, the photogenerated holes at VB of MoS_2 tend to be transferred to HOMO of PPy. The CO_2 photocatalytic reduction into CH_4 and CO gas occurs at PPy because it has appropriate CB potentials ($E_{LUMO,\ PPy}$ = -1.15 V vs. NHE). The accumulated holes in the VB of MoS_2 participate in reactions with H_2O to produce protons

(H^+) and oxygen (O_2). The electrons in CB of MoS_2 can participate in the production of H_2 using protons. Due to its excellent electron storage capability and conductivity properties, rGO would trap photogenerated electrons from the CB of MoS_2 or PPy, enhancing electron separation and transfer for improved photocatalytic reduction. Overall, the photoreduction of CO_2 into CO, CH_4, and H_2 production can be expressed by below equations:

$$rGO\text{-}MoS_2/PPy + h\nu \longrightarrow rGO\text{-}MoS_2/PPy\ (e_{CB}^{-}\text{-}h_{VB}^{+})$$

$$PPy\ (e_{HOMO}^{-}\text{—}h_{LUMIO}^{+}) \longrightarrow PPy\ (h_{LUMO}^{+}) + PPy\ (e_{HOMO}^{-})$$

$$MoS_2\ (e_{CB}^{-}\text{-}h_{VB}^{+}) \longrightarrow MoS_2\ (h_{VB}^{+}) + MoS_2\ (e_{CB}^{-})$$

$$2H_2O + MoS_2\ (4h_{VB}^{+}) \longrightarrow 4H^+ + O_2 \quad E^0 = +0.82\ V$$

$$CO_2 + 2H^+ + PPy\ (2e_{LUMO}^{-}) \longrightarrow CO + H_2O \quad E^0 = -0.53\ V$$

$$CO_2 + 8H^+ + PPy\ (8e_{LUMO}^{-}) \longrightarrow CH_4 + 2H_2O \quad E^0 = -0.24\ V$$

$$2H^+ + MoS_2 \text{ or } PPy\ (2e_{CB/LUMO}^{-}) \longrightarrow H_2 \quad E^0 = -0.41\ V$$

The formation of CO gas takes place via the reaction of CO_2 radical anions (bent $CO_2^{\bullet -}$) with the generated protons. CO demonstrates a durable affinity for N-containing surfaces such as PPy, which prevent the desorption of CO molecules from the surface. During the course of the reaction, these CO molecules can accept additional electrons and react with H^+ to form intermediates (CH_xO_y) such as carbene or formyl radicals and finally produce CH_4.[75] The hydrogen generation potential from water is -0.41V vs. NHE (pH = 7), and reduction potentials of photocatalytic CO_2 conversion reactions range from -0.2 to -0.7 V vs. NHE (pH =7). Therefore, the photoreduction of CO_2 competes with the reduction of water during the process. In the present case, the protons required for the production of CH_4 are obtained from the limited water molecules adsorbed on the surface of rGO-MoS_2/PPy-150, which is sufficient for the production of CH_4, which involves eight protons. In contrast, the production of CO requires two protons from water. Thus, the main reaction products of the photocatalytic conversion of

CO_2 on rGO-MoS_2/PPy-150 nanocomposite are CO and CH_4 rather than higher hydrocarbons (CH_3OH, C_2H_5OH, HCHO, and HCOOH). Moreover, the reduction potential for the conversion of CO_2 to CH_4 is more positive than that of the conversion of CO_2 to CO, which may lead to backward electron-transfer from CH_4 to the oxidized species, consequently affecting the production rate of CH_4 via more intricate reactions.

4. Conclusion

In summary, rGO-MoS_2 and polypyrrole (rGO-MoS_2/PPy) nanocomposites were successfully constructed by a facile wet chemical route that utilized GO as an initial precursor. The resulting nanocomposite demonstrated distinctively enhanced optical and conductive properties as well as notably improved photocatalytic reduction of CO_2 into CH_4, CO, and H_2. The nanocomposite containing an optimum amount of PPy (rGO-MoS_2/PPy-150) exhibited the highest efficiency for the photocatalytic reduction of CO_2 using liquid water to CO (3.95 μmol g^{-1} h^{-1}), CH_4 (1.50 μmol g^{-1} h^{-1}), and H_2 (4.19 μmol g^{-1} h^{-1}). The improvement in the photocatalytic performance of the highly active surface material rGO-MoS_2/PPy-150 was attributed to the synergistic effect of the MoS_2, rGO and PPy nanostructures, which promoted the separation and migration of the photogenerated charges through the heterojunction interfaces and decreased electron-hole recombination. Owing to its excellent conductivities, CO_2 adsorption capabilities via its amine groups, and electron storage properties, the PPy in the rGO-MoS_2/PPy nanocomposite performed multiple roles in enhancing the photocatalytic reduction of CO_2. The lower content of PPy in nanocomposite affords better catalytic performance. Moreover, importantly, the good recycling performance of the rGO-MoS_2/PPy-150 nanocomposite demonstrated the durability and stability of the photocatalyst. Thus, this study has introduced an advanced rationally designed non-noble metal photocatalyst based on

conducting materials (PPy and rGO) for high-performance photoreduction of CO_2 into renewable fuels.

Acknowledgments

The authors (NR, RG, and SSR) would like to thank the Council for Scientific and Industrial Research (HGER74P) and Department of Science and Innovation (HGERA8X) for financial support. The authors SK and SE would like to thank the EPSRC EP/R035407/2 grant for funding.

References

1. Khalil, M.; Gunlazuardi, J.; Ivandini, T. A.; Umar, A., Photocatalytic conversion of CO2 using earth-abundant catalysts: A review on mechanism and catalytic performance. *Renewable and Sustainable Energy Reviews* 2019, *113*, 109246.
2. Koytsoumpa, E. I.; Bergins, C.; Kakaras, E., The CO2 economy: Review of CO2 capture and reuse technologies. *The Journal of Supercritical Fluids* 2018, *132*, 3-16.
3. Li, X.; Yu, J.; Jaroniec, M.; Chen, X., Cocatalysts for Selective Photoreduction of CO2 into Solar Fuels. *Chemical Reviews* 2019, *119* (6), 3962-4179.
4. Zhu, S.; Wang, D., Photocatalysis: Basic Principles, Diverse Forms of Implementations and Emerging Scientific Opportunities. *Advanced Energy Materials* 2017, *7* (23), 1700841.
5. Michl, J., Photochemical CO 2 reduction: Towards an artificial leaf? *Nature chemistry* 2011, *3* (4), 268.
6. Qin, J.; Wang, S.; Ren, H.; Hou, Y.; Wang, X., Photocatalytic reduction of CO2 by graphitic carbon nitride polymers derived from urea and barbituric acid. *Applied Catalysis B: Environmental* 2015, *179*, 1-8.
7. Izumi, Y., Recent advances in the photocatalytic conversion of carbon dioxide to fuels with water and/or hydrogen using solar energy and beyond. *Coordination Chemistry Reviews* 2013, *257* (1), 171-186.
8. Kim, J.; Kwon, E. E., Photoconversion of carbon dioxide into fuels using semiconductors. *Journal of CO2 Utilization* 2019, *33*, 72-82.
9. Gusain, R.; Kumar, P.; Sharma, O. P.; Jain, S. L.; Khatri, O. P., Reduced graphene oxide–CuO nanocomposites for photocatalytic conversion of CO2 into methanol under visible light irradiation. *Applied Catalysis B: Environmental* 2016, *181*, 352-362.
10. Tonda, S.; Kumar, S.; Bhardwaj, M.; Yadav, P.; Ogale, S., g-C3N4/NiAl-LDH 2D/2D Hybrid Heterojunction for High-Performance Photocatalytic Reduction of CO2 into Renewable Fuels. *ACS Applied Materials & Interfaces* 2018, *10* (3), 2667-2678.
11. Das, S.; Wan Daud, W. M. A., A review on advances in photocatalysts towards CO2 conversion. *RSC Advances* 2014, *4* (40), 20856-20893.
12. Wang, C.; Sun, Z.; Zheng, Y.; Hu, Y. H., Recent progress in visible light photocatalytic conversion of carbon dioxide. *Journal of Materials Chemistry A* 2019, *7* (3), 865-887.

13. Sun, Z.; Talreja, N.; Tao, H.; Texter, J.; Muhler, M.; Strunk, J.; Chen, J., Catalysis of Carbon Dioxide Photoreduction on Nanosheets: Fundamentals and Challenges. *Angewandte Chemie International Edition* 2018, *57* (26), 7610-7627.
14. Chen, Y.; Jia, G.; Hu, Y.; Fan, G.; Tsang, Y. H.; Li, Z.; Zou, Z., Two-dimensional nanomaterials for photocatalytic CO2 reduction to solar fuels. *Sustainable Energy & Fuels* 2017, *1* (9), 1875-1898.
15. Luo, B.; Liu, G.; Wang, L., Recent advances in 2D materials for photocatalysis. *Nanoscale* 2016, *8* (13), 6904-6920.
16. Gusain, R.; Kumar, N.; Ray, S. S., Recent advances in carbon nanomaterial-based adsorbents for water purification. *Coordination Chemistry Reviews* 2020, *405*, 213111.
17. Tsai, M.-L.; Su, S.-H.; Chang, J.-K.; Tsai, D.-S.; Chen, C.-H.; Wu, C.-I.; Li, L.-J.; Chen, L.-J.; He, J.-H., Monolayer MoS2 Heterojunction Solar Cells. *ACS Nano* 2014, *8* (8), 8317-8322.
18. Joshi, N.; Hayasaka, T.; Liu, Y.; Liu, H.; Oliveira, O. N.; Lin, L., A review on chemiresistive room temperature gas sensors based on metal oxide nanostructures, graphene and 2D transition metal dichalcogenides. *Microchimica Acta* 2018, *185* (4), 213.
19. Wu, Y.; Joshi, N.; Zhao, S.; Long, H.; Zhou, L.; Ma, G.; Peng, B.; Oliveira Jr, O. N.; Zettl, A.; Lin, L., NO2 gas sensors based on CVD tungsten diselenide monolayer. *Applied Surface Science* 2020, *529*, 147110.
20. Liu, Y.; Peng, X., Recent advances of supercapacitors based on two-dimensional materials. *Applied Materials Today* 2017, *8*, 104-115.
21. Meier, A. J.; Garg, A.; Sutter, B.; Kuhn, J. N.; Bhethanabotla, V. R., MoS2 Nanoflowers as a Gateway for Solar-Driven CO2 Photoreduction. *ACS Sustainable Chemistry & Engineering* 2019, *7* (1), 265-275.
22. Kumar, N.; Fosso-Kankeu, E.; Ray, S. S., Achieving Controllable MoS2 Nanostructures with Increased Interlayer Spacing for Efficient Removal of Pb(II) from Aquatic Systems. *ACS Applied Materials & Interfaces* 2019, *11* (21), 19141-19155.
23. Kumari, S.; Mungse, H. P.; Gusain, R.; Kumar, N.; Sugimura, H.; Khatri, O. P., Octadecanethiol-grafted molybdenum disulfide nanosheets as oil-dispersible additive for reduction of friction and wear. *FlatChem* 2017, *3*, 16-25.
24. Gusain, R.; Kumar, N.; Fosso-Kankeu, E.; Ray, S. S., Efficient Removal of Pb(II) and Cd(II) from Industrial Mine Water by a Hierarchical MoS2/SH-MWCNT Nanocomposite. *ACS Omega* 2019, *4* (9), 13922-13935.
25. Malkappa, K.; Ray, S. S.; Kumar, N., Enhanced Thermo-Mechanical Stiffness, Thermal Stability, and Fire Retardant Performance of Surface-Modified 2D MoS2 Nanosheet-Reinforced Polyurethane Composites. *Macromolecular Materials and Engineering* 2019, *304* (1), 1800562.
26. Kumar, N.; George, B. P. A.; Abrahamse, H.; Parashar, V.; Ngila, J. C., Sustainable one-step synthesis of hierarchical microspheres of PEGylated MoS2 nanosheets and MoO3 nanorods: Their cytotoxicity towards lung and breast cancer cells. *Applied Surface Science* 2017, *396*, 8-18.
27. Wang, H.; Tran, D.; Qian, J.; Ding, F.; Losic, D., MoS2/Graphene Composites as Promising Materials for Energy Storage and Conversion Applications. *Advanced Materials Interfaces* 2019, *6* (20), 1900915.
28. Umukoro, E. H.; Kumar, N.; Ngila, J. C.; Arotiba, O. A., Expanded graphite supported p-n MoS2-SnO2 heterojunction nanocomposite electrode for enhanced photo-electrocatalytic degradation of a pharmaceutical pollutant. *Journal of Electroanalytical Chemistry* 2018, *827*, 193-203.
29. Wang, M.; Ju, P.; Li, J.; Zhao, Y.; Han, X.; Hao, Z., Facile Synthesis of MoS2/g-C3N4/GO Ternary Heterojunction with Enhanced Photocatalytic Activity for Water Splitting. *ACS Sustainable Chemistry & Engineering* 2017, *5* (9), 7878-7886.
30. Kumar, S.; Sahoo, P. K.; Satpati, A. K., Electrochemical and SECM Investigation of MoS2/GO and MoS2/rGO Nanocomposite Materials for HER Electrocatalysis. *ACS Omega* 2017, *2* (11), 7532-7545.

31. Ding, Y.; Zhou, Y.; Nie, W.; Chen, P., MoS2–GO nanocomposites synthesized via a hydrothermal hydrogel method for solar light photocatalytic degradation of methylene blue. *Applied Surface Science* 2015, *357*, 1606-1612.
32. Li, X.; Shen, R.; Ma, S.; Chen, X.; Xie, J., Graphene-based heterojunction photocatalysts. *Applied Surface Science* 2018, *430*, 53-107.
33. Deng, Z. H.; Li, L.; Ding, W.; Xiong, K.; Wei, Z. D., Synthesized ultrathin MoS2 nanosheets perpendicular to graphene for catalysis of hydrogen evolution reaction. *Chemical Communications* 2015, *51* (10), 1893-1896.
34. Ma, C.-B.; Qi, X.; Chen, B.; Bao, S.; Yin, Z.; Wu, X.-J.; Luo, Z.; Wei, J.; Zhang, H.-L.; Zhang, H., MoS2 nanoflower-decorated reduced graphene oxide paper for high-performance hydrogen evolution reaction. *Nanoscale* 2014, *6* (11), 5624-5629.
35. Saravanan, R.; Sacari, E.; Gracia, F.; Khan, M. M.; Mosquera, E.; Gupta, V. K., Conducting PANI stimulated ZnO system for visible light photocatalytic degradation of coloured dyes. *Journal of Molecular Liquids* 2016, *221*, 1029-1033.
36. Yang, Y.; Wen, J.; Wei, J.; Xiong, R.; Shi, J.; Pan, C., Polypyrrole-Decorated Ag-TiO2 Nanofibers Exhibiting Enhanced Photocatalytic Activity under Visible-Light Illumination. *ACS Applied Materials & Interfaces* 2013, *5* (13), 6201-6207.
37. Marcano, D. C.; Kosynkin, D. V.; Berlin, J. M.; Sinitskii, A.; Sun, Z.; Slesarev, A.; Alemany, L. B.; Lu, W.; Tour, J. M., Improved synthesis of graphene oxide. *ACS nano* 2010, *4* (8), 4806-4814.
38. Verma, S.; Mungse, H. P.; Kumar, N.; Choudhary, S.; Jain, S. L.; Sain, B.; Khatri, O. P., Graphene oxide: an efficient and reusable carbocatalyst for aza-Michael addition of amines to activated alkenes. *Chemical Communications* 2011, *47* (47), 12673-12675.
39. Stobinski, L.; Lesiak, B.; Malolepszy, A.; Mazurkiewicz, M.; Mierzwa, B.; Zemek, J.; Jiricek, P.; Bieloshapka, I., Graphene oxide and reduced graphene oxide studied by the XRD, TEM and electron spectroscopy methods. *Journal of Electron Spectroscopy and Related Phenomena* 2014, *195*, 145-154.
40. Thangappan, R.; Kalaiselvam, S.; Elayaperumal, A.; Jayavel, R.; Arivanandhan, M.; Karthikeyan, R.; Hayakawa, Y., Graphene decorated with MoS2 nanosheets: a synergetic energy storage composite electrode for supercapacitor applications. *Dalton Transactions* 2016, *45* (6), 2637-2646.
41. Wang, K.; Li, L.; Liu, Y.; Zhang, C.; Liu, T., Constructing a “Pizza-Like” MoS2/Polypyrrole/Polyaniline Ternary Architecture with High Energy Density and Superior Cycling Stability for Supercapacitors. *Advanced Materials Interfaces* 2016, *3* (19), 1600665.
42. Nanda, S. S.; Yi, D. K.; Kim, K., Study of antibacterial mechanism of graphene oxide using Raman spectroscopy. *Scientific Reports* 2016, *6* (1), 28443.
43. Kumar, N.; Mittal, H.; Alhassan, S. M.; Ray, S. S., Bionanocomposite Hydrogel for the Adsorption of Dye and Reusability of Generated Waste for the Photodegradation of Ciprofloxacin: A Demonstration of the Circularity Concept for Water Purification. *ACS Sustainable Chemistry & Engineering* 2018, *6* (12), 17011-17025.
44. Mungse, H. P.; Verma, S.; Kumar, N.; Sain, B.; Khatri, O. P., Grafting of oxo-vanadium Schiff base on graphene nanosheets and its catalytic activity for the oxidation of alcohols. *Journal of Materials Chemistry* 2012, *22* (12), 5427-5433.
45. Zhang, X.; Zhang, J.; Song, W.; Liu, Z., Controllable Synthesis of Conducting Polypyrrole Nanostructures. *The Journal of Physical Chemistry B* 2006, *110* (3), 1158-1165.
46. Tang, H.; Wang, J.; Yin, H.; Zhao, H.; Wang, D.; Tang, Z., Growth of Polypyrrole Ultrathin Films on MoS2 Monolayers as High-Performance Supercapacitor Electrodes. *Advanced Materials* 2015, *27* (6), 1117-1123.
47. Ryu, Z.; Zheng, J.; Wang, M.; Zhang, B., Characterization of pore size distributions on carbonaceous adsorbents by DFT. *Carbon* 1999, *37* (8), 1257-1264.
48. Caliman, C. C.; Mesquita, A. F.; Cipriano, D. F.; Freitas, J. C. C.; Cotta, A. A. C.; Macedo, W. A. A.; Porto, A. O., One-pot synthesis of amine-functionalized graphene oxide by microwave-assisted

reactions: an outstanding alternative for supporting materials in supercapacitors. *RSC Advances* 2018, *8* (11), 6136-6145.
49. Lian, M.; Wu, X.; Wang, Q.; Zhang, W.; Wang, Y., Hydrothermal synthesis of Polypyrrole/MoS2 intercalation composites for supercapacitor electrodes. *Ceramics International* 2017, *43* (13), 9877-9883.
50. Lu, X.; Lin, Y.; Dong, H.; Dai, W.; Chen, X.; Qu, X.; Zhang, X., One-Step Hydrothermal Fabrication of Three-dimensional MoS2 Nanoflower using Polypyrrole as Template for Efficient Hydrogen Evolution Reaction. *Scientific Reports* 2017, *7* (1), 42309.
51. Eslava, S.; Baklanov, M. R.; Neimark, A. V.; Iacopi, F.; Kirschhock, C. E. A.; Maex, K.; Martens, J. A., Evidence of Large Voids in Pure-Silica-Zeolite Low-k Dielectrics Synthesized by Spin-on of Nanoparticle Suspensions. *Advanced Materials* 2008, *20* (16), 3110-3116.
52. Basavaraja, C.; Kim, W. J.; Thinh, P. X.; Huh, D. S., Electrical conductivity studies on water-soluble polypyrrole–graphene oxide composites. *Polymer Composites* 2011, *32* (12), 2076-2083.
53. Liu, J.; Mu, X.; Yang, Y.; Chen, F.; Wang, J.; Li, Y.; Wang, B., Construct 3D Pd@MoS2-conjugated polypyrrole framworks Heterojunction with unprecedented photocatalytic activity for Tsuji-Trost reaction under visible light. *Applied Catalysis B: Environmental* 2019, *244*, 356-366.
54. Liu, W.; Yang, X.; Zhang, Y.; Xu, M.; Chen, H., Ultra-stable two-dimensional MoS2 solution for highly efficient organic solar cells. *RSC Advances* 2014, *4* (62), 32744-32748.
55. Tabačiarová, J.; Mičušík, M.; Fedorko, P.; Omastová, M., Study of polypyrrole aging by XPS, FTIR and conductivity measurements. *Polymer Degradation and Stability* 2015, *120*, 392-401.
56. Garg, K.; Shanmugam, R.; Ramamurthy, P. C., Synthesis, characterisationand optical studies of new tetraethyl- rubyrin-graphene oxide covalent adducts. *Optical Materials* 2018, *76*, 42-47.
57. Rabchinskii, M. K.; Dideikin, A. T.; Kirilenko, D. A.; Baidakova, M. V.; Shnitov, V. V.; Roth, F.; Konyakhin, S. V.; Besedina, N. A.; Pavlov, S. I.; Kuricyn, R. A.; Lebedeva, N. M.; Brunkov, P. N.; Vul', A. Y., Facile reduction of graphene oxide suspensions and films using glass wafers. *Scientific Reports* 2018, *8* (1), 14154.
58. Sharma, N.; Das, T.; Kumar, S.; Bhosale, R.; Kabir, M.; Ogale, S., Photocatalytic Activation and Reduction of CO2 to CH4 over Single Phase Nano Cu3SnS4: A Combined Experimental and Theoretical Study. *ACS Applied Energy Materials* 2019, *2* (8), 5677-5685.
59. Kumar, N.; Sinha Ray, S.; Ngila, J. C., Ionic liquid-assisted synthesis of Ag/Ag2Te nanocrystals via a hydrothermal route for enhanced photocatalytic performance. *New Journal of Chemistry* 2017, *41* (23), 14618-14626.
60. Mishra, A. K.; Lakshmi, K. V.; Huang, L., Eco-friendly synthesis of metal dichalcogenides nanosheets and their environmental remediation potential driven by visible light. *Scientific Reports* 2015, *5* (1), 15718.
61. Liu, G.; Ma, H.; Teixeira, I.; Sun, Z.; Xia, Q.; Hong, X.; Tsang, S. C. E., Hydrazine-Assisted Liquid Exfoliation of MoS2 for Catalytic Hydrodeoxygenation of 4-Methylphenol. *Chemistry – A European Journal* 2016, *22* (9), 2910-2914.
62. Ahmad, R.; Srivastava, R.; Yadav, S.; Singh, D.; Gupta, G.; Chand, S.; Sapra, S., Functionalized Molybdenum Disulfide Nanosheets for 0D–2D Hybrid Nanostructures: Photoinduced Charge Transfer and Enhanced Photoresponse. *The Journal of Physical Chemistry Letters* 2017, *8* (8), 1729-1738.
63. Liu, P.; Liu, Y.; Ye, W.; Ma, J.; Gao, D., Flower-like N-doped MoS2for photocatalytic degradation of RhB by visible light irradiation. *Nanotechnology* 2016, *27* (22), 225403.
64. Su, C.; Wang, L.; Xu, L.; Zhang, C., Synthesis of a novel ferrocene-contained polypyrrole derivative and its performance as a cathode material for Li-ion batteries. *Electrochimica Acta* 2013, *104*, 302-307.
65. Wang, Q. H.; Kalantar-Zadeh, K.; Kis, A.; Coleman, J. N.; Strano, M. S., Electronics and optoelectronics of two-dimensional transition metal dichalcogenides. *Nature Nanotechnology* 2012, *7* (11), 699-712.

66. Zheng, B.; Chen, Y., Controllable Growth of Monolayer MoS2 and MoSe2 Crystals Using Three-temperature-zone Furnace. *IOP Conference Series: Materials Science and Engineering* 2017, *274*, 012085.
67. Kim, T.; Shin, J. C., Structural defects in a nanomesh of bulk MoS2 using an anodic aluminum oxide template for photoluminescence efficiency enhancement. *Scientific Reports* 2018, *8*, 6648.
68. Lin, X.; Xing, J.; Wang, W.; Shan, Z.; Xu, F.; Huang, F., Photocatalytic activities of heterojunction semiconductors Bi2O3/BaTiO3: a strategy for the design of efficient combined photocatalysts. *J. Phys. Chem. C* 2007, *111* (49), 18288-18293.
69. Xu, J.; Hu, Y.; Zeng, C.; Zhang, Y.; Huang, H., Polypyrrole decorated BiOI nanosheets: Efficient photocatalytic activity for treating diverse contaminants and the critical role of bifunctional polypyrrole. *Journal of colloid and interface science* 2017, *505*, 719-727.
70. Li, F.; Jiang, X.; Zhao, J.; Zhang, S., Graphene oxide: A promising nanomaterial for energy and environmental applications. *Nano Energy* 2015, *16*, 488-515.
71. Chandra, V.; Yu, S. U.; Kim, S. H.; Yoon, Y. S.; Kim, D. Y.; Kwon, A. H.; Meyyappan, M.; Kim, K. S., Highly selective CO2 capture on N-doped carbon produced by chemical activation of polypyrrole functionalized graphene sheets. *Chemical communications* 2012, *48* (5), 735-737.
72. An, X.; Li, K.; Tang, J., Cu2O/reduced graphene oxide composites for the photocatalytic conversion of CO2. *ChemSusChem* 2014, *7* (4), 1086-1093.
73. Kuehnel, M. F.; Orchard, K. L.; Dalle, K. E.; Reisner, E., Selective Photocatalytic CO2 Reduction in Water through Anchoring of a Molecular Ni Catalyst on CdS Nanocrystals. *Journal of the American Chemical Society* 2017, *139* (21), 7217-7223.
74. Chaudhary, Y. S.; Woolerton, T. W.; Allen, C. S.; Warner, J. H.; Pierce, E.; Ragsdale, S. W.; Armstrong, F. A., Visible light-driven CO2 reduction by enzyme coupled CdS nanocrystals. *Chemical Communications* 2012, *48* (1), 58-60.
75. Liu, Z.; Wang, Z.; Qing, S.; Xue, N.; Jia, S.; Zhang, L.; Li, L.; Li, N.; Shi, L.; Chen, J., Improving methane selectivity of photo-induced CO2 reduction on carbon dots through modification of nitrogen-containing groups and graphitization. *Applied Catalysis B: Environmental* 2018, *232*, 86-92.